Atmospheric
Chemistry
and Physics

Composited analyses of the chemical and physical characteristics of co-polluted days by ozone and PM$_{2.5}$ over 2013–2020 in the Beijing–Tianjin–Hebei region

Huibin Dai[1], **Hong Liao**[1], **Ke Li**[1], **Xu Yue**[1], **Yang Yang**[1], **Jia Zhu**[1], **Jianbing Jin**[1], **Baojie Li**[1], and **Xingwen Jiang**[2]

[1]Jiangsu Key Laboratory of Atmospheric Environment Monitoring and Pollution Control, Jiangsu Collaborative Innovation Center of Atmospheric Environment and Equipment Technology, School of Environmental Science and Engineering, Nanjing University of Information Science and Technology, Nanjing 210044, China
[2]Institute of Plateau Meteorology, China Meteorological Administration, Chengdu, Sichuan 610072, China

Correspondence: Hong Liao (hongliao@nuist.edu.cn)

Abstract. The co-polluted days by ozone (O$_3$) and PM$_{2.5}$ (particulate matter with an aerodynamic equivalent diameter of 2.5 μm or less) (O$_3$–PM$_{2.5}$PDs) were frequently observed in the Beijing–Tianjin–Hebei (BTH) region in warm seasons (April–October) of 2013–2020. We applied the 3-D global chemical transport model (GEOS-Chem) to investigate the chemical and physical characteristics of O$_3$–PM$_{2.5}$PDs by composited analyses of such days that were captured by both the observations and the model. Model results showed that, when O$_3$–PM$_{2.5}$PDs occurred, the concentrations of hydroxyl radical and total oxidant, sulfur oxidation ratio, and nitrogen oxidation ratio were all high, and the concentrations of sulfate at the surface were the highest among all pollution types. We also found unique features in vertical distributions of aerosols during O$_3$–PM$_{2.5}$PDs; concentrations of PM$_{2.5}$ decreased with altitude near the surface but remained stable at 975–819 hPa. Process analyses showed that secondary aerosols (nitrate, ammonium, and sulfate) had strong chemical productions at 913–819 hPa, which were then transported downward, resulting in the quite uniform vertical profiles at 975–819 hPa on O$_3$–PM$_{2.5}$PDs. The weather patterns for O$_3$–PM$_{2.5}$PDs were characterized by anomalous high-pressure system at 500 hPa as well as strong southerlies and high RH at 850 hPa. The latter resulted in the strong chemical productions around 850 hPa on O$_3$–PM$_{2.5}$PDs. The physical and chemical characteristics of O$_3$–PM$_{2.5}$PDs are quite different from those of polluted days by either O$_3$ alone or PM$_{2.5}$ alone and have important implications for air quality management.

1 Introduction

Surface ozone (O$_3$) and PM$_{2.5}$ (particulate matter with an aerodynamic equivalent diameter of 2.5 μm or less) are important air pollutants in the atmosphere that have harmful effects on public health (Gao and Ji, 2018; Jiang et al., 2019), ecosystems (Ren et al., 2011; Yue et al., 2017), and crops (Wang et al., 2005, 2007). Surface O$_3$ is a secondary pollutant produced by photochemical oxidation of volatile organic compounds (VOCs) and nitrogen oxides (NO$_x \equiv$ NO + NO$_2$) in the presence of intense ultraviolet light, and the major PM$_{2.5}$ components (nitrate, NO$_3^-$; am-

monium, NH$_4^+$; sulfate, SO$_4^{2-}$; black carbon, BC; and organic carbon, OC) are mainly caused by anthropogenic emissions of aerosols and aerosol precursors. Although surface O$_3$ and PM$_{2.5}$ have different formation mechanisms, they are coupled through the common precursors (NO$_x$ and VOCs) and photochemical reactions (Chu et al., 2020). Since 2013, stringent clean air actions have been implemented to improve air quality in China (Chinese State Council, 2013, 2018). However, O$_3$ concentrations increased unexpectedly, while PM$_{2.5}$ concentrations decreased drastically in the past years (M. Li et al., 2019). The co-polluted days by O$_3$ and PM$_{2.5}$ (concentrations of both O$_3$ and PM$_{2.5}$ exceed the national air qual-

ity standards on the same day, hereafter referred to as O_3–$PM_{2.5}$PDs) were also reported (Dai et al., 2021). Therefore, it is fundamental to examine the chemical and physical characteristics of O_3–$PM_{2.5}$PDs.

The Beijing–Tianjin–Hebei (BTH) region is the most populated region in northern China. In the past few years, concentrations of O_3 and $PM_{2.5}$ in BTH were among the highest in China. The observations from China National Environmental Monitoring Center (CNEMC) showed that the mean and maximum MDA8 (daily maximum 8 h average) O_3 in North China in summer of 2019 were 83 and 129 ppb, respectively, and the summer mean MDA8 O_3 increased with a trend of 3.3 ppb a^{-1} over 2013–2019 (Li et al., 2020). Gong et al. (2020) reported that O_3-polluted days (i.e., MDA8 O_3 concentration exceeds 80 ppb) in May–July in BTH increased from 35 d in the year 2014 to 56 d in 2018. As for observed $PM_{2.5}$, the concentration averaged over BTH had a decreasing trend of 10 µg m^{-3} yr^{-1} over 2013–2019, and the mean value was 79 ± 17 µg m^{-3} over these years (Li et al., 2020). BTH also had the highest frequency and intensity of severe-haze-pollution days (i.e., days with daily mean $PM_{2.5}$ concentration exceeding 150 µg m^{-3}) in China from 2013 to 2017, with an observed mean frequency of 21.2 d yr^{-1} and an observed mean intensity of 231.6 µg m^{-3} (Dang and Liao, 2019).

The interactions between O_3 and $PM_{2.5}$ have been reported in previous studies. Zhu et al. (2019) examined the spatiotemporal characteristics of the correlations between observed O_3 and $PM_{2.5}$ at 1497 sites in China for 2016 and found that O_3–$PM_{2.5}$ had the highest positive correlations (correlation coefficients $> +0.7$) in July in southern China and the largest negative correlations (r values < -0.5) during January in northern China. K. Li et al. (2019) used the GEOS-Chem model to analyze the O_3–$PM_{2.5}$ relationship in northern China and found that O_3 production was suppressed under high-$PM_{2.5}$ conditions ($PM_{2.5}$ concentrations > 60 µg m^{-3}) because of the reactive uptake of hydrogen oxide radicals (HO_x) by aerosol particles. Chu et al. (2020) analyzed the observed daily $PM_{2.5}$ and O_3 concentrations in 114 cities in China during the years of 2013–2018 and found that the correlations between O_3 and $PM_{2.5}$ tended to change from negative in 2013 to positive in 2018 in China as air quality improved.

Few previous studies have examined the co-occurrence of O_3 and $PM_{2.5}$ pollution (MDA8 $O_3 > 80$ ppb and $PM_{2.5} > 75$ µg m^{-3}). Zong et al. (2021) used the obliquely rotated principal component analysis in the T-mode (T-PCA) method to identify the synoptic weather pattern associated with O_3–$PM_{2.5}$PDs in eastern China during summer of 2015–2018 and found that O_3–$PM_{2.5}$PDs were associated with a stable western Pacific subtropical high ridge, which brought warm and moist airflow from the East China Sea to eastern China to promote hygroscopic growth of fine particulate matter in BTH and the northern Yangtze River Delta (YRD). Dai et al. (2021) analyzed O_3–$PM_{2.5}$PDs in

the YRD for April–October of 2013–2019 by using observations and reported that the co-polluted days occurred mainly in April (29.6 % of co-polluted days occurred in April), May (23.0 %), June (19.5 %), and October (10.8 %) under meteorological conditions of higher relative humidity, higher surface air temperature, and lower wind speed relative to the days with O_3 pollution alone. Qin et al. (2021) investigated O_3–$PM_{2.5}$PDs by using the hourly observed concentrations of water-soluble ions, OC, and elemental carbon (EC) in 2019 in cities of Nanjing and Changzhou. They found that inorganic aerosols mainly existed as NH_4NO_3, and the correlation coefficients between the secondary components NO_3^-, NH_4^+, and SO_4^{2-} were relatively high during O_3–$PM_{2.5}$PDs in 2019, indicating a significant formation of secondary inorganic aerosols. Although these studies have discussed the meteorological conditions and some chemical characteristics of O_3–$PM_{2.5}$PDs, the understanding of O_3–$PM_{2.5}$PDs was quite limited because of the limited observations of chemical species involved.

In this work, we take advantage of the comprehensive chemical mechanism of the global chemical transport model to have better understanding of O_3–$PM_{2.5}$PDs. We apply the 3-D global chemical transport model (GEOS-Chem) to simulate O_3–$PM_{2.5}$PDs in BTH in the years of 2013–2020 and investigate the chemical and physical characteristics of O_3–$PM_{2.5}$PDs by composited analyses of such days that are captured by both the observations and the model. The objectives of this study are (1) to examine the underlying chemical mechanisms for O_3–$PM_{2.5}$PDs in BTH for warm seasons (April–October) of 2013–2020 by comparing O_3–$PM_{2.5}$PDs with polluted days by O_3 alone or by $PM_{2.5}$ alone and (2) to identify the weather patterns that are associated with O_3–$PM_{2.5}$PDs in BTH. The observations, the reanalyzed meteorological data, the GEOS-Chem model, and the process analysis are described in Sect. 2. The observed O_3–$PM_{2.5}$PDs are presented in Sect. 3.1. The evaluation of simulated concentrations of O_3 and $PM_{2.5}$ as well as the simulated pollution days by O_3 and/or $PM_{2.5}$ are shown in Sect. 3.2. The underlying mechanisms of O_3–$PM_{2.5}$PDs are shown in Sect. 3.3. In Sect. 3.4, the meteorological conditions for the co-occurrence of O_3 and $PM_{2.5}$ pollution are investigated. The conclusions are presented in Sect. 4.

2 Methods

2.1 Observed O_3 and $PM_{2.5}$ concentrations

Hourly concentrations of $PM_{2.5}$ and O_3 in China over the years of 2013–2020 were taken from the public website of CNEMC (https://air.cnemc.cn:18007/, last access: 17 November 2022). To ensure data quality, the daily mean $PM_{2.5}$ concentration was calculated when there were valid data for more than 20 h during that day, and the MDA8 O_3 concentration was calculated when there were valid data for at least 6 h for each 8 h. For the calculation of monthly and

annual mean concentrations, the number of days with valid concentrations had to be more than 15 in each month. The spatial distribution of the 79 valid sites within BTH (37–41° N, 114–118° E; the black rectangle) is shown in Fig. 1. For model evaluation, the observed concentrations were averaged over sites within each of the 0.5° latitude × 0.625° longitude Modern-Era Retrospective analysis for Research and Applications (MERRA-2) grid cells. There are 18 model grids in BTH. Note that the observed O_3 concentrations from this network have a unit of micrograms per cubic meter. For the consistency of observed and simulated O_3 concentrations, $1 \mu g \, m^{-3}$ of O_3 is approximately 0.5 ppb under the conditions of 298 K and 1013 hPa. The observed O_3 concentrations reported by the CNEMC were under standard conditions of 273 K and 1013 hPa before 31 August 2018 and were under standard conditions of 298 K and 1013 hPa afterwards (http://www.mee.gov.cn/xxgk2018/xxgk/xxgk01/201808/t20180815_629602.html, last access: 17 November 2022), which were accounted for as O_3 concentrations were converted to parts per billion.

According to the National Ambient Air Quality Standard of China (GB3095-2012), O_3 ($PM_{2.5}$) concentration exceeds the national air quality standard if the MDA8 O_3 (daily mean $PM_{2.5}$) concentration is higher than $160 \mu g \, m^{-3}$ ($75 \mu g \, m^{-3}$). In this study, we define O_3 polluted days (hereafter called "O_3PDs") for days with MDA8 O_3 concentration $> 160 \mu g \, m^{-3}$, $PM_{2.5}$ polluted days (hereafter called "$PM_{2.5}$PDs") as days with daily mean $PM_{2.5}$ concentration $> 75 \mu g \, m^{-3}$, and the co-pollution days by O_3 and $PM_{2.5}$ (O_3–$PM_{2.5}$PDs) as days with daily MDA8 O_3 concentration $> 160 \mu g \, m^{-3}$ as well as a daily mean $PM_{2.5}$ concentration $> 75 \mu g \, m^{-3}$.

2.2 Reanalyzed meteorological fields

Meteorological fields were obtained from MERRA-2, which were generated by the NASA Global Modeling and Assimilation Office (GMAO). The MERRA-2 data have a horizontal resolution of 0.5° latitude × 0.625° longitude and 72 vertical layers (Molod et al., 2015). To analyze the meteorological conditions for O_3–$PM_{2.5}$PDs, vertical pressure velocity (OMEGA), planetary boundary layer height (PBLH), temperature (T), relative humidity (RH), and surface incoming shortwave flux (SWGDN) are used. Note that the temporal resolution for PBLH, T, and SWGDN is 1 h, and that for OMEGA and RH is 3 h. Daily mean geopotential heights at 850 and 500 hPa from the National Center for Environmental Prediction (NCEP) and National Center for Atmospheric Research (NCAR) global reanalysis with a resolution of 2.5° latitude by 2.5° longitude are also utilized in this study.

2.3 Observed aerosol optical depth

We obtained the version 3 datasets of observed daily aerosol optical depth (AOD) of level 2 (improved cloud screening and quality-assured) from the Aerosol Robotic Network (AERONET; https://aeronet.gsfc.nasa.gov/new_web/index.html, last access: 17 November 2022) established by NASA and LOA-PHOTONS (Giles et al., 2019). Three sites in the BTH region have observations available over 2013–2020, including Beijing (39.97° N, 116.38° E), Beijing-CAMS (39.93° N, 116.31° E), and Xianghe (39.75° N, 116.96° E). The AOD values at 440 and 675 nm at these three sites are analyzed in this study.

2.4 GEOS-Chem model

We simulated O_3 and $PM_{2.5}$ using the nested version of the 3-D global chemical transport model (GEOS-Chem, version 11-01) driven by the MERRA-2 meteorological data. The nested domain was set over Asia (11° S–55° N, 60–150° E) with a horizontal resolution of 0.5° latitude × 0.625° longitude, and the chemical boundary conditions were provided by the global GEOS-Chem simulation with 2.5° latitude × 2.5° longitude horizontal resolution.

The GEOS-Chem model includes fully coupled O_3–NO_x–hydrocarbon and an aerosol chemistry mechanism (Bey et al., 2001; Pye et al., 2009) to simulate aerosols including SO_4^{2-} (Park et al., 2004), NO_3^- (Pye et al., 2009), NH_4^+, BC and OC (Park et al., 2003), mineral dust (Fairlie et al., 2007), and sea salt (Alexander et al., 2005) as well as the gas-phase pollutants such as NO_x and O_3. Over the Asian domain, the anthropogenic emissions of OC, BC, carbon monoxide (CO), sulfur dioxide (SO_2), NO_x, ammonia (NH_3), and VOCs were obtained from the Multi-resolution Emission Inventory for China (MEIC), which includes emissions from the industry, power, residential, and transportation sectors for the years of 2014–2017 (Li et al., 2017; Zheng et al., 2018), 2019, and 2020 (Zheng et al., 2021). Emissions in 2018 were obtained by the interpolation of those in 2017 and 2019 for each grid due to the lack of publicly accessible emission inventories for that year. The biogenic emissions in GEOS-Chem are simulated using MEGAN v2.1 (Guenther et al., 2012).

The hourly O_3 and $PM_{2.5}$ concentrations for the years of 2013–2020 were simulated by the GEOS-Chem model and were driven by MERRA-2 meteorological fields. The model was spun up for 6 months before the integration over the studied time period.

2.5 Process analysis

Process analysis (PA) was applied to identify the relative importance of atmospheric processes on O_3–$PM_{2.5}$PDs. PA has been widely used in previous studies to examine the key processes contributing to air pollution episodes (Gonçalves et al., 2009; Dang and Liao, 2019; Gong and Liao, 2019) as well as the interannual and decadal variations in air pollutants
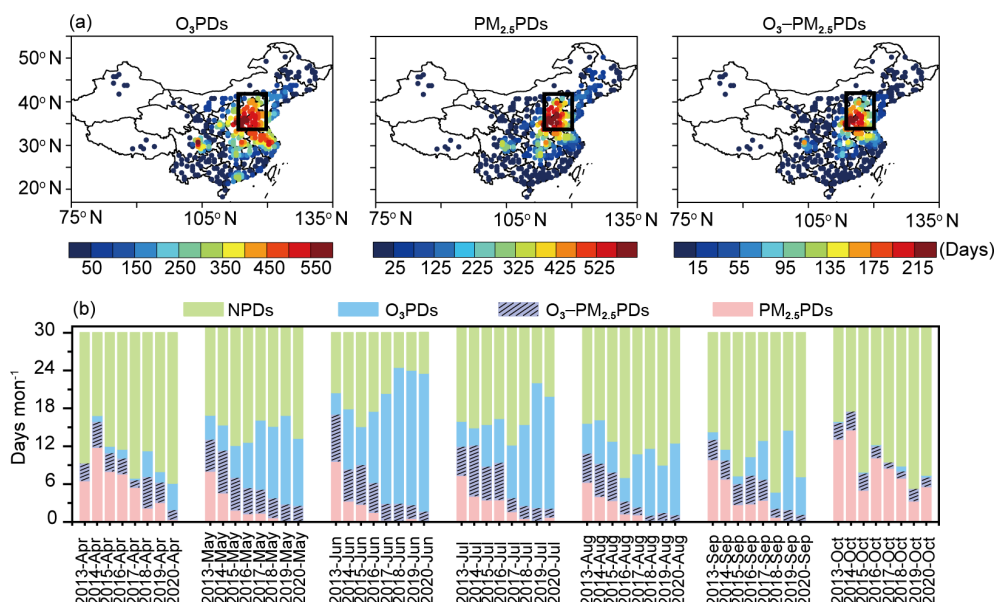
Figure 1. (a) Spatial distributions of observed numbers of O_3PDs, $PM_{2.5}$PDs, and O_3–$PM_{2.5}$PDs summed over April–October of 2013–2020. The solid black rectangle indicates the BTH region. **(b)** The observed numbers of NPDs (non-polluted days, green), O_3PDs (blue and purple with slashes), O_3–$PM_{2.5}$PDs (purple with slashes), and $PM_{2.5}$PDs (pink and purple with slashes) averaged over all sites in BTH from April to October in 2013 to 2020.

(Mu and Liao, 2014; Lou et al., 2015). Five major processes that influence O_3 and $PM_{2.5}$ concentrations were diagnosed at every time step, including net chemical production, dry deposition, horizontal advection, vertical advection, and diffusion, for the regional pollution days (days with more than half of the sites in BTH experiencing pollution). We carried out PA for O_3SPDs (excluding O_3–$PM_{2.5}$PDs from O_3PDs), $PM_{2.5}$SPDs (excluding O_3–$PM_{2.5}$PDs from $PM_{2.5}$PDs), and O_3–$PM_{2.5}$PDs over BTH.

3 Results

3.1 Observed polluted days by O_3 and $PM_{2.5}$

Figure 1a shows the spatial distributions of observed numbers of O_3PDs, $PM_{2.5}$PDs, and O_3–$PM_{2.5}$PDs summed over the warm seasons (April–October) of 2013–2020. The spatial distributions of polluted days in each year are shown in Fig. S1 in the Supplement. The numbers of O_3PDs, $PM_{2.5}$PDs, and O_3–$PM_{2.5}$PDs were high in BTH, which were, respectively, 524.3 344.6, and 128.1 d from observations, as the values were averaged over all sites in BTH. The high numbers of O_3PDs, $PM_{2.5}$PDs, and O_3–$PM_{2.5}$PDs in BTH were associated with the highest anthropogenic emissions (NO_x and non-methane volatile organic compounds, NMVOCs) in this region (Dang et al., 2021).

Figure 1b shows the numbers of days averaged over all sites in BTH for non-polluted days (NPDs; MDA8 $O_3 < 80$ ppb and $PM_{2.5} < 75$ µg m^{-3}), O_3PDs, O_3–$PM_{2.5}$PDs, and $PM_{2.5}$PDs in each month of warm seasons

from 2013 to 2020. O_3PDs and O_3–$PM_{2.5}$PDs mainly occurred in May, June, and July, while $PM_{2.5}$PDs mainly appeared in April and October. The monthly numbers of O_3–$PM_{2.5}$PDs ($PM_{2.5}$PDs) declined from 2013 to 2020, with the fastest drop in June, from 7.5 (17.1) d in June 2013 to 1.8 (1.8) d in June 2020. In contrast, the numbers of O_3PDs kept increasing, especially in June, from 10.9 d in June 2013 to 23.6 d in June 2020. The reductions in O_3–$PM_{2.5}$PDs were associated with the large reductions in $PM_{2.5}$ since the implementation of the Clean Air Action in 2013.

Figure 2a shows the linear trends of observed O_3PDs, $PM_{2.5}$PDs, and O_3–$PM_{2.5}$PDs in warm seasons of 2013–2020 averaged over BTH. O_3PDs showed an upward trend of 7.9 d yr^{-1} from 2013 to 2020. However, the numbers of $PM_{2.5}$PDs and O_3–$PM_{2.5}$PDs decreased over 2013–2020, with linear trends of -11.2 and -3.4 d yr^{-1}, respectively. Figure 2b shows the changes in percentage of O_3–$PM_{2.5}$PDs on $PM_{2.5}$PDs from 2013 to 2020 for each month. It should be noted that, when $PM_{2.5}$PDs occurred, the proportions of O_3–$PM_{2.5}$PDs had an upward trend from 2013 to 2020. In May, June, August, and September of 2020, the proportions of O_3–$PM_{2.5}$PDs on $PM_{2.5}$PDs reached 100 %, indicating that $PM_{2.5}$ pollution was accompanied by O_3 pollution in recent years.
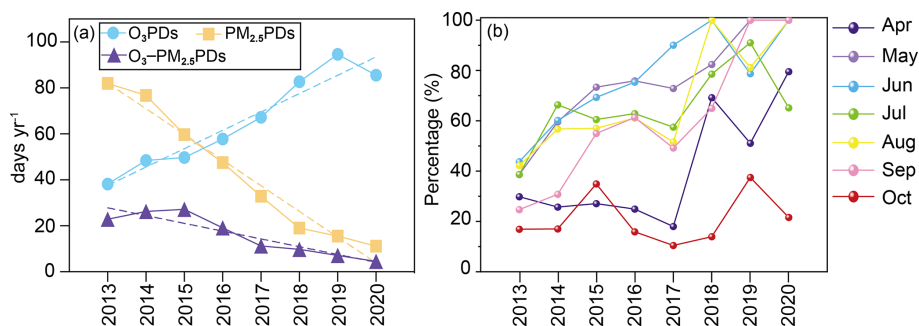
Figure 2. (a) The trends of observed O_3PDs, $PM_{2.5}$PDs, and O_3–$PM_{2.5}$PDs in warm seasons from 2013 to 2020 averaged over all sites in BTH. The blue, yellow, and purple solid lines (dashed lines) represent the numbers (liner trend) of O_3PDs, $PM_{2.5}$PDs, and O_3–$PM_{2.5}$PDs, respectively. **(b)** The percentage of O_3–$PM_{2.5}$PDs on $PM_{2.5}$PDs for April to October in 2013 to 2020. The polluted days were averaged over all sites in BTH.

3.2 Simulated polluted days and model evaluation

3.2.1 Simulated surface-layer MDA8 O_3 and $PM_{2.5}$ concentrations

Figure 3a and b show, respectively, the spatial distributions of simulated and observed surface-layer concentrations of MDA8 O_3 and $PM_{2.5}$ in China, as the concentrations are averaged over the warm seasons (April–October) of 2013–2020. The concentrations of MDA8 O_3 and $PM_{2.5}$ were both high in BTH. Averaged over BTH and the studied time period, the observed concentrations of MDA8 O_3 and $PM_{2.5}$ were 58.1 ppb and 60.3 $\mu g\,m^{-3}$, respectively, while the simulated values were 68.0 ppb and 61.1 $\mu g\,m^{-3}$, respectively. Figure 3c and d compare the time series of observed and simulated daily MDA8 O_3 and $PM_{2.5}$ concentrations averaged over BTH. The simulated daily concentrations of MDA8 O_3 ($PM_{2.5}$) in eight warm seasons have a normalized mean bias (NMB) of 7.9 % (10.6 %). The model generally captures the daily variations (peaks and troughs) in the observed MDA8 O_3 and $PM_{2.5}$ concentrations, with R values of 0.80 and 0.72, respectively. It should be noted that mineral dust and sea-salt aerosols were not considered in this study because they are not the major aerosol components in China, and the concentrations are generally low based on previous measurements (Xuan et al., 2000; Ye et al., 2003; Duan et al., 2006; Zhao et al., 2013). However, excluding dust and sea salt may lead to low biases in simulated $PM_{2.5}$ concentrations.

Due to the lack of publicly accessible long-term observations of $PM_{2.5}$ components in China, we compared the simulated SO_2 and NO_2 (precursors for SO_4^{2-} and NO_3^-) with observations from CNEMC in Fig. S2. The simulated daily mean concentrations of NO_2 (SO_2) agree well with the observations from CNEMC, with R of 0.82 (0.78) and NMB of −14.9 % (9.3 %).

3.2.2 Simulated O_3PDs, $PM_{2.5}$PDs, and O_3–$PM_{2.5}$PDs

Figure S3 shows the capability of the model in capturing the polluted days. Although the GEOS-Chem model well reproduces the spatial distributions of observed MDA8 O_3 and $PM_{2.5}$ concentrations, it underestimates the numbers of O_3PDs, $PM_{2.5}$PDs, and O_3–$PM_{2.5}$PDs because of the model's deficiency in capturing the peak concentrations of air pollutants. Such deficiency was also reported in previous studies that used the GEOS-Chem model or the weather Research and Forecasting with Chemistry (WFR-chem) model (Zhang and Wang, 2016; Ni et al., 2018; Gong and Liao, 2019; Dang and Liao, 2019). Therefore, to identify O_3PDs, $PM_{2.5}$PDs, and O_3–$PM_{2.5}$PDs using model results, we utilized lower thresholds by considering the NMBs of simulated MDA8 O_3 and $PM_{2.5}$ concentrations in each of the 18 grids of BTH. Taking the grid of Beijing as an example, simulated MDA8 O_3 and $PM_{2.5}$ had NMBs of −22.0 % and −26.9 %, respectively, as the simulated concentrations were compared with observations for days with observed concentrations higher than the national air quality standards over the warm seasons of 2013–2020. We then adjusted the threshold of O_3PDs in this grid to be 62.4 ppb (80 ppb × 78 %) and that of $PM_{2.5}$PDs to be 54.8 $\mu g\,m^{-3}$ (75 $\mu g\,m^{-3}$ × 73.1 %). These adjusted thresholds were also used to identify O_3–$PM_{2.5}$PDs. Such an approach was also used in previous studies to better capture the pollution events based on the simulations (Dang and Liao, 2019; Gong and Liao, 2019). With the adjusted thresholds, 56 %–93 % of the observed O_3PDs, $PM_{2.5}$PDs, and O_3–$PM_{2.5}$PDs can be captured by the model (Fig. S3e).

3.2.3 Simulated O_3SPDs, $PM_{2.5}$SPDs, and O_3–$PM_{2.5}$PDs

Since O_3PDs or $PM_{2.5}$PDs encompasses O_3–$PM_{2.5}$PDs, we further define O_3 single pollution days (hereafter called "O_3SPDs", which exclude O_3–$PM_{2.5}$PDs from O_3PDs) and $PM_{2.5}$ single pollution days (hereafter called "$PM_{2.5}$SPDs", which exclude O_3–$PM_{2.5}$PDs from $PM_{2.5}$PDs) for the pur-
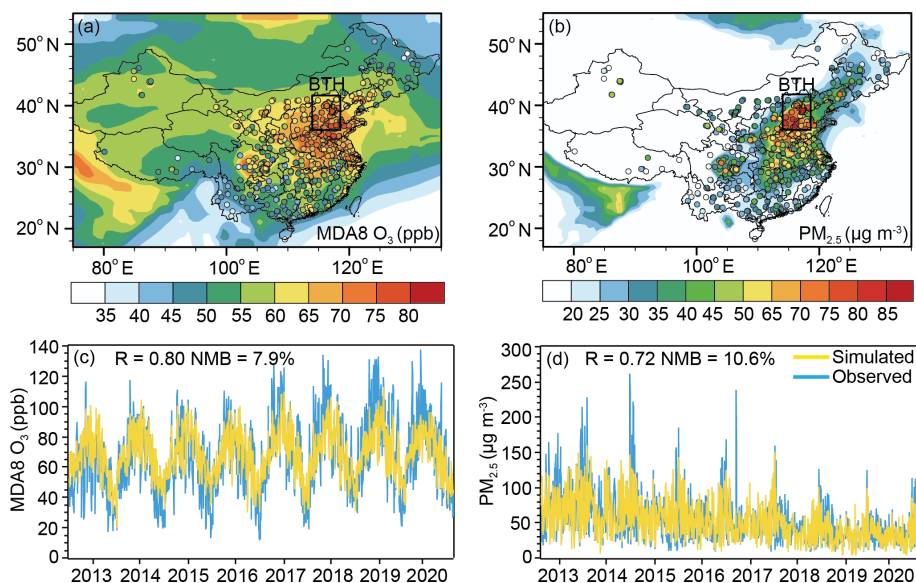
Figure 3. Spatial distributions of simulated (shades) and observed (CNEMC, dots) surface-layer concentrations of **(a)** MDA8 O_3 (ppb) and **(b)** $PM_{2.5}$ ($\mu g\,m^{-3}$) averaged over the eight warm seasons (April to October, 2013–2020). The solid black rectangle in **(a)** and **(b)** indicates the BTH region. Simulated and observed daily concentrations of surface-layer **(c)** MDA8 O_3 and **(d)** $PM_{2.5}$ averaged over BTH. The correlation coefficient (R) and normalized mean bias (NMB) are also shown for **(c)** and **(d)**. $\text{NMB} = \left(\sum_{i=1}^{N} (M_i - O_i) / \sum_{i=1}^{N} (O_i) \right) \times 100\,\%$, where O_i and M_i are the observed and simulated concentrations, respectively; i refers to the ith day, and N is the total number of days.

pose of obtaining the characteristics of different polluted days. Figure 4a and b show, respectively, the spatial distributions of numbers of $O_3\text{SPDs}$, $PM_{2.5}\text{SPDs}$, and O_3–$PM_{2.5}\text{PDs}$ from observations and from the GEOS-Chem model using the adjusted thresholds. Considering the total of polluted days in 18 grids in BTH, observed $O_3\text{SPDs}$, $PM_{2.5}\text{SPDs}$, and O_3–$PM_{2.5}\text{PDs}$ were, respectively, 3937, 3698, and 2024 d, in which 75.0 % (2954/3937), 58.1 % (2148/3698), and 79.7 % (1614/2024) were captured by observation and simulation simultaneously (Fig. 4c). In addition, the numbers of observed and captured $O_3\text{SPDs}$, $PM_{2.5}\text{SPDs}$, and O_3–$PM_{2.5}\text{PDs}$ in each month are shown in Fig. S4. The model has a fairly good capability of capturing the observed polluted days in each month.

3.3 Chemical characteristics of polluted days by O_3 and $PM_{2.5}$

In this section, to investigate the chemical characteristics of $O_3\text{SPDs}$, $PM_{2.5}\text{SPDs}$, and O_3–$PM_{2.5}\text{PDs}$, we present first the simulated atmospheric oxidants in Sect. 3.3.1 and then show the simulated surface concentrations and vertical profiles of $PM_{2.5}$ and MDA8 O_3 in Sect. 3.3.2 and 3.3.3, respectively, followed by the process analysis in Sect. 3.3.4. The observed AOD values to verify the model results are presented in Sect. 3.3.5.

3.3.1 Atmospheric oxidants of $O_3\text{SPDs}$, $PM_{2.5}\text{SPDs}$, and O_3–$PM_{2.5}\text{PDs}$

Figure 5 shows the boxplots of daily concentrations of hydroxyl radical (OH) and total oxidant ($O_x = O_3 + NO_2$) from the model for days of $O_3\text{SPDs}$, $PM_{2.5}\text{SPDs}$, and O_3–$PM_{2.5}\text{PDs}$ that were observed and also captured by the model (samples in Fig. 4b) in the warm seasons of 2013–2020 in 18 grids of BTH. The levels of OH and O_x characterize the atmospheric oxidation capacity, following Liu et al. (2020) and Nan et al. (2017). The concentrations of OH were the highest on $O_3\text{SPDs}$, with an averaged value of 2.8×10^6 molec. cm^{-3}, followed by that on O_3–$PM_{2.5}\text{PDs}$ (2.0×10^6 molec. cm^{-3}) and on $PM_{2.5}\text{SPDs}$ (1.0×10^6 molec. cm^{-3}). Due to the lack of publicly accessible observations of OH in BTH, we compare the simulated OH concentrations with observations reported in the literature (Table S1). The simulated OH concentrations agree closely with the observed values. In Wangdu of BTH, while the observed daily maximum OH concentrations in summer of 2014 were in the range of 5–15×10^6 molec. cm^{-3} (Tan et al., 2017), the simulated OH concentrations in the same time period in this work were 3.7–9.5×10^6 molec. cm^{-3}. In Beijing in summer of 2017, the observed daily mean OH concentration was 5.8×10^6 molec. cm^{-3} (Woodward-Massey et al., 2020), and our simulated value was 2.4×10^6 molec. cm^{-3}.
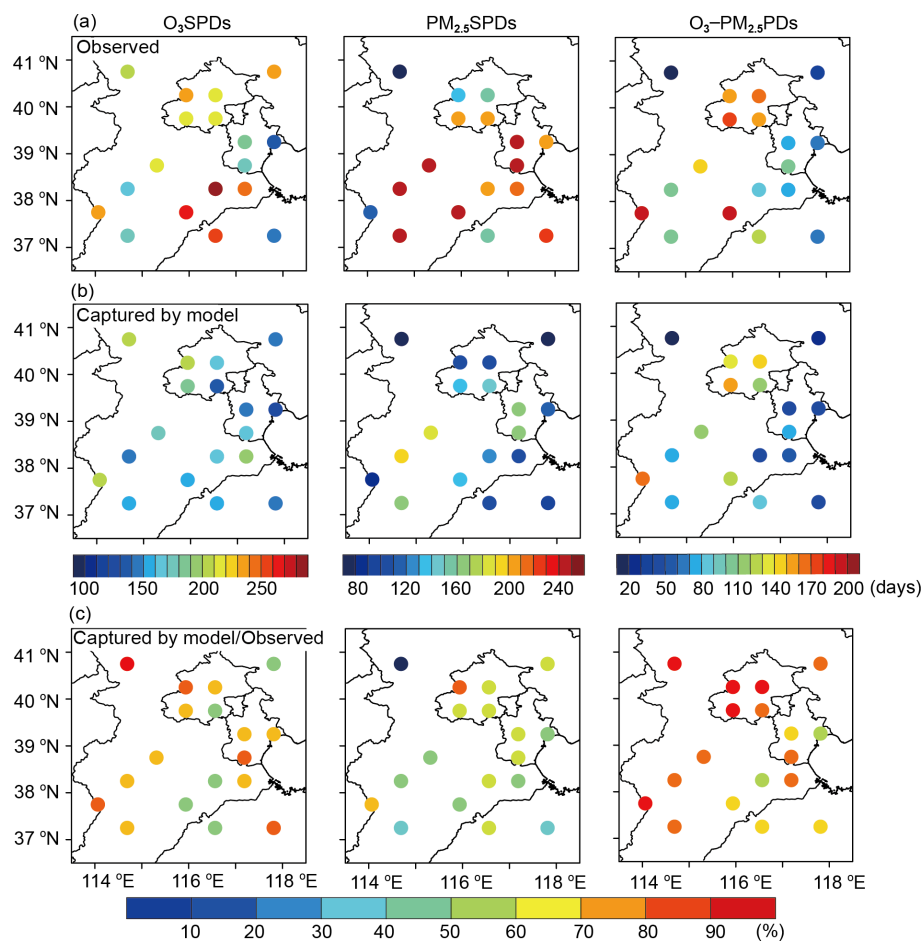
Figure 4. Spatial distributions of **(a)** observed numbers of O_3SPDs, $PM_{2.5}$SPDs, and O_3–$PM_{2.5}$PDs; **(b)** numbers of polluted days that were observed and also captured by the GEOS-Chem model with adjusted thresholds; and **(c)** percentages of observed polluted days that were captured by the model with adjusted thresholds. The values were calculated for the warm months (April to October) of 2013–2020.
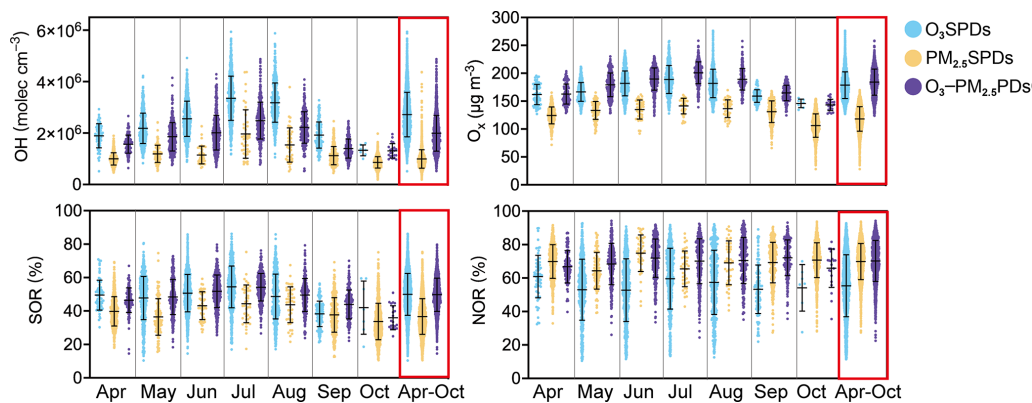

Figure 5. The boxplots of surface-layer hydroxyl radical (OH, molec. cm^{-3}), total oxidant (O_x, µg m^{-3}), sulfur oxidation ratio (SOR, %), and nitrogen oxidation ratio (NOR, %) for model-captured O_3SPDs, $PM_{2.5}$SPDs, and O_3–$PM_{2.5}$PDs in 18 grids of BTH in the months of April to October from 2013 to 2020. The whiskers represent the standard deviation, and the black line represents the mean value of the samples.

The mean values of O_x were, respectively, 178.7, 118.1, and 184.1 µg m^{-3} on O_3SPDs, $PM_{2.5}$SPDs, and O_3–$PM_{2.5}$PDs, indicating that the atmospheric oxidation capacity was strong on O_3–$PM_{2.5}$PDs, which favored the production of secondary components of $PM_{2.5}$. Figure 5 also shows sulfur oxidation ratio (SOR; n-SO_4^{2-} / (n-SO_4^{2-} + n-SO_2), where n-SO_4^{2-} and n-SO_2 are the concentrations of SO_4^{2-} and SO_2, respectively) and nitrogen oxidation ratio (NOR; n-NO_3^- / (n-NO_3^- + n-NO_2), where n-NO_3^- and n-NO_2 are the concentrations of NO_3^- and NO_2, respectively). SOR and NOR are measures of the conversion degrees of sulfur and nitrogen, respectively (Zhu et al., 2019). On O_3SPDs, $PM_{2.5}$SPDs, and O_3–$PM_{2.5}$PDs, the averaged values of SOR were 50.0 %, 36.7 %, and 49.7 %, and those of NOR were 55.4 %, 70.0 %, and 70.2 %, respectively. The high SOR and NOR on O_3–$PM_{2.5}$PDs indicated the strong formation of SO_4^{2-} and NO_3^- that was promoted by high atmospheric oxidation capacity. The monthly variations in OH, O_x, and SOR were similar (Fig. 5), with the highest values in summer, owing to the high temperature that promoted high concentrations of oxidants and SOR. It is interesting that SOR and O_x values were higher on O_3–$PM_{2.5}$PDs than on O_3SPDs or on $PM_{2.5}$SPDs during May–August. Similarly, NOR values were higher on O_3–$PM_{2.5}$PDs than on O_3SPDs or on $PM_{2.5}$SPDs in May and July–September. Overall, the O_3–$PM_{2.5}$PDs occurred with high levels of atmospheric oxidants, SOR, and NOR, leading to combined increases in O_3 and $PM_{2.5}$ concentrations.

3.3.2　Surface-layer concentrations of $PM_{2.5}$ components on O_3SPDs, $PM_{2.5}$SPDs, and O_3–$PM_{2.5}$PDs

The simulated concentrations of $PM_{2.5}$ components (NO_3^-, NH_4^+, SO_4^{2-}, BC, and OC, averaged over 18 grids of BTH, are shown in Fig. 6 for O_3SPDs, $PM_{2.5}$SPDs, and O_3–$PM_{2.5}$PDs in the warm seasons of 2013–2020 that were observed and also captured by the model. While the mean concentrations of NO_3^-, NH_4^+, BC, and OC were all the highest on $PM_{2.5}$SPDs, SO_4^{2-} concentration was the highest on O_3–$PM_{2.5}$PDs. On O_3SPDs, $PM_{2.5}$SPDs, and O_3–$PM_{2.5}$PDs, the mean concentrations of SO_4^{2-} were 6.2, 9.4, and 11.97 µg m^{-3}, respectively, and the percentages of SO_4^{2-} in $PM_{2.5}$ were 14.9 %, 9.0 %, and 15.0 %, respectively. In July and August, the concentrations of SO_4^{2-} and MDA8 O_3 on O_3–$PM_{2.5}$PDs were the highest compared with those on O_3SPDs and $PM_{2.5}$SPDs (Fig. S5).

Figure 7 presents the hourly concentrations of NO_3^-, NH_4^+, SO_4^{2-}, BC, OC, and O_3 for model-captured O_3SPDs, $PM_{2.5}$SPDs, and O_3–$PM_{2.5}$PDs over all 18 grids of BTH in the warm seasons from 2013–2020. Concentrations of NO_3^- and NH_4^+ had similarities in diurnal variations, all of which reached the highest values in the early morning (05:00 local time, LT, on O_3SPDs and O_3–$PM_{2.5}$PDs, 07:00–08:00 LT
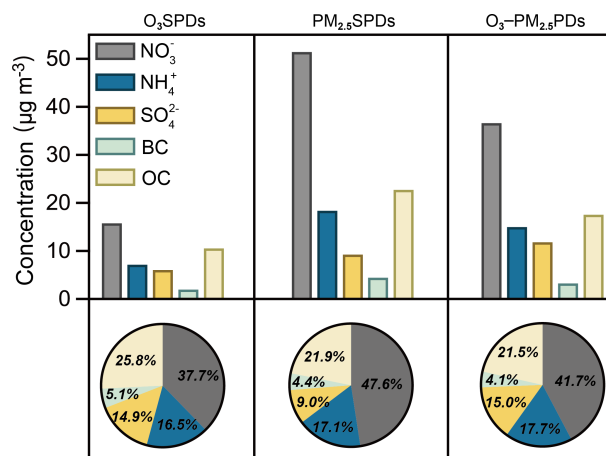

Figure 6. The concentrations of $PM_{2.5}$ components (µg m^{-3}) and percentages of $PM_{2.5}$ components (%) at the surface for NO_3^-, NH_4^+, SO_4^{2-}, BC, and OC. The values were averaged over the model-captured O_3SPDs, $PM_{2.5}$SPDs, and O_3–$PM_{2.5}$PDs in the months of April to October of 2013–2020 in BTH.

on $PM_{2.5}$SPDs) and had the lowest values in the late afternoon (18:00 LT on O_3SPDs and O_3–$PM_{2.5}$PDs, 16:00 LT on $PM_{2.5}$SPDs). Concentrations of BC and OC peaked at the same time as those of NO_3^- and NH_4^+ and had the lowest values at 15:00 LT on O_3SPDs, $PM_{2.5}$SPDs, and O_3–$PM_{2.5}$PDs. The diurnal variations in NO_3^-, NH_4^+, BC, and OC, which generally reached their highest concentrations before the sudden uplift of PBLH in the early morning (times for uplift of PBLH: 06:00 LT on O_3SPDs and O_3–$PM_{2.5}$PDs, 07:00 LT on $PM_{2.5}$SPDs), reflected the diurnal variations in PBLH (shown in Fig. S6). Compared to O_3SPDs and O_3–$PM_{2.5}$PDs, the PBLH of $PM_{2.5}$SPDs was lower and uplifted 1 h later, which was more favorable for the accumulation of aerosols. During the daytime, PBLH on O_3–$PM_{2.5}$PDs was between O_3SPDs and $PM_{2.5}$SPDs.

It is worth noting that the diurnal variations in SO_4^{2-} were different from those of other aerosol species, with the highest values at 20:00, 09:00, and 16:00 LT on O_3SPDs, $PM_{2.5}$SPDs, and O_3–$PM_{2.5}$SPDs, respectively, and the lowest values in early morning and night (05:00 LT on O_3SPDs and O_3–$PM_{2.5}$PDs, 23:00 LT on $PM_{2.5}$SPDs). For the diurnal variation in O_3, the highest values occurred during the daytime (16:00 LT on O_3SPDs and O_3–$PM_{2.5}$PDs, 15:00 LT on $PM_{2.5}$SPDs), and the lowest values appeared at 05:00 LT in all cases. Therefore, on O_3–$PM_{2.5}$PDs, the time of the highest value of SO_4^{2-} was the same as that of O_3, indicating that SO_4^{2-} and O_3 were produced synergistically during the daytime with strong atmospheric oxidation.
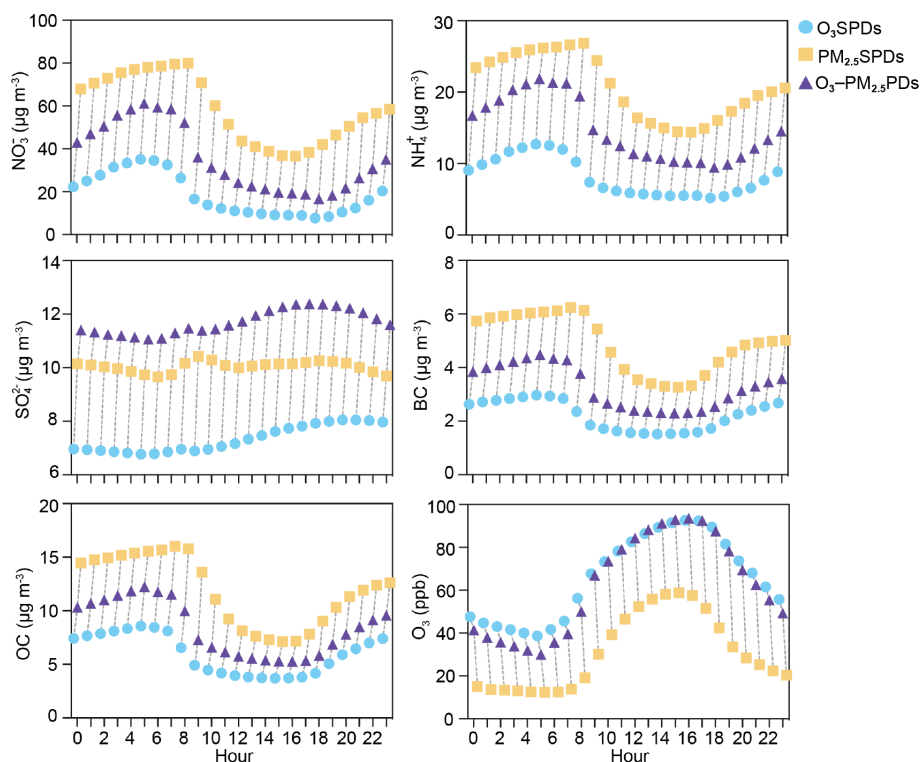
Figure 7. The hourly concentrations of NO_3^-, NH_4^+, SO_4^{2-}, BC, OC, and O_3 averaged over the model-captured O_3SPDs, $PM_{2.5}$SPDs, and O_3–$PM_{2.5}$PDs in BTH in the months of April to October of 2013–2020.

3.3.3 Vertical distributions of O_3 and $PM_{2.5}$ on O_3SPDs, $PM_{2.5}$SPDs, and O_3–$PM_{2.5}$PDs

The simulated vertical distributions of O_3 and $PM_{2.5}$ averaged over the 18 grids of BTH and the O_3SPDs, $PM_{2.5}$SPDs, and O_3–$PM_{2.5}$PDs in warm seasons of 2013–2020 are shown in Fig. 8. The vertical distribution of O_3 on O_3SPDs was similar to that on O_3–$PM_{2.5}$PDs (Fig. 8a). In these two cases, concentrations of O_3 increased from the surface to about 975 hPa, remained high between 975 and 819 hPa and decreased with altitude between 819 and 663 hPa. Although the magnitudes of O_3 were close at the surface (61.9 ppb on O_3–$PM_{2.5}$PDs and 58.1 ppb on O_3SPDs), the concentration of O_3 averaged over 975 and 819 hPa was 10.4 % higher on O_3–$PM_{2.5}$PDs than on O_3SPDs, which was a very unique feature of O_3–$PM_{2.5}$PDs. For the case of $PM_{2.5}$SPDs, the concentrations of O_3 were the lowest among the three cases and increased gently with altitude above 975 hPa.

Figure 8b shows the vertical distributions of $PM_{2.5}$ components. In all the cases, $PM_{2.5}$ concentrations were the highest at the surface, and decreased with altitude from the surface to 975 hPa. However, concentrations of $PM_{2.5}$ were quite stable between 975 and 819 hPa for O_3SPDs (about 36.4 µg m^{-3}) and O_3–$PM_{2.5}$PDs (about 58.1 µg m^{-3}), corresponding to the stable O_3 levels at these altitudes in these two cases (Fig. 8a). For $PM_{2.5}$SPDs, while $PM_{2.5}$ concentration at the surface was the highest among the three cases, it decreased rapidly

between 975 and 819 hPa. The averaged $PM_{2.5}$ concentration between 975 and 819 hPa was 52.4 µg m^{-3} on $PM_{2.5}$SPDs, which was lower than that on O_3–$PM_{2.5}$PDs.

To further investigate the differences in vertical profiles of NO_3^-, NH_4^+, SO_4^{2-}, BC, OC, and $PM_{2.5}$ on O_3SPDs, $PM_{2.5}$SPDs, and O_3–$PM_{2.5}$PDs, the ratios of concentration at 975 hPa to that at the surface as well as the concentration at 819 hPa to that at 975 hPa are shown in Table 1. The concentration of $PM_{2.5}$ decreased largely, with the ratio of $PM_{2.5(975\,hPa)}$ / $PM_{2.5(1005\,hPa)}$ of 0.78 on O_3–$PM_{2.5}$PDs and of 0.74 on $PM_{2.5}$SPDs. For each of the $PM_{2.5}$ components, the ratios near the surface (from 1005 to 975 hPa, shaded gray area in Fig. 8) were close in the three types of pollution. While the ratios of NO_3^-, NH_4^+, BC, and OC were in the range of 0.65–0.80, the ratios of SO_4^{2-} were about 0.93–0.98, indicating that SO_4^{2-} concentrations were quite uniform from the surface to 975 hPa in all three types of pollution.

In the upper layers (975–819 hPa, red rectangle in Fig. 8), the changes in concentrations of pollutants with altitude on $PM_{2.5}$SPDs were quite different from those on O_3–$PM_{2.5}$PDs and O_3SPDs. The decline in $PM_{2.5}$ from 975 to 819 hPa was slow on O_3–$PM_{2.5}$PDs ($PM_{2.5(819\,hPa)}$ / $PM_{2.5(975\,hPa)}$ = 0.89) and O_3SPDs (0.86) and fast on $PM_{2.5}$SPDs (0.67). Considering that the variation in BC with altitude was mainly driven by meteorology (Sun et al., 2020), the vertical variations in other components
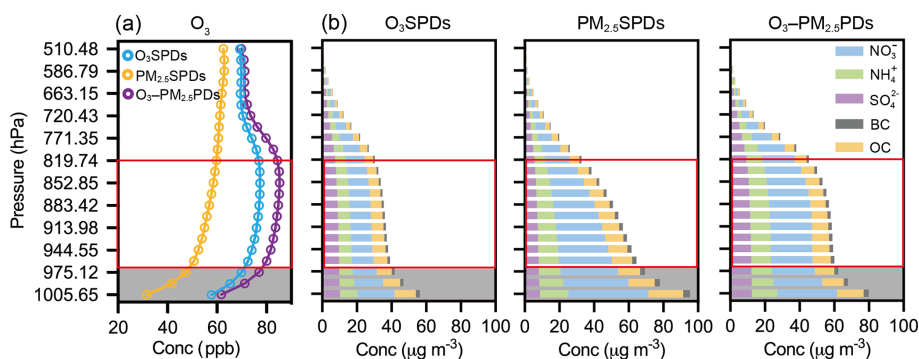
Figure 8. The vertical distributions of **(a)** concentrations of O_3 (ppb) and **(b)** $PM_{2.5}$ components ($\mu g\,m^{-3}$) of NO_3^-, NH_4^+, SO_4^{2-}, BC, OC averaged over the model-captured O_3SPDs, $PM_{2.5}$SPDs, and O_3–$PM_{2.5}$PDs in BTH in the months of April to October of 2013–2020.

Table 1. The ratios at 975 and 1005 hPa (shaded gray area in Fig. 8) and at 819 and 975 hPa (red frame in Fig. 8) of NO_3^-, NH_4^+, SO_4^{2-}, BC, OC, and $PM_{2.5}$ on O_3SPDs, $PM_{2.5}$SPDs, and O_3–$PM_{2.5}$PDs in BTH region.

		NO_3^-	NH_4^+	SO_4^{2-}	BC	OC	$PM_{2.5}$
$Conc_{819\,hPa}$ / $Conc_{975\,hPa}$	O_3SPDs	0.95	0.90	0.85	0.73	0.73	0.86
	$PM_{2.5}$SPDs	0.64	0.68	0.81	0.64	0.63	0.67
	O_3–$PM_{2.5}$PDs	0.94	0.91	0.87	0.79	0.77	0.89
$Conc_{975\,hPa}$ / $Conc_{1005\,hPa}$	O_3SPDs	0.65	0.77	0.96	0.69	0.70	0.74
	$PM_{2.5}$SPDs	0.72	0.76	0.93	0.67	0.65	0.73
	O_3–$PM_{2.5}$PDs	0.72	0.80	0.98	0.76	0.73	0.78

that differed significantly from BC indicated the influences of chemical processes. On $PM_{2.5}$SPDs, NO_3^-, NH_4^+, and OC had about the same ratio as BC (0.64) (with large decreases with height), except for SO_4^{2-} concentration, which had a ratio of 0.81. On O_3–$PM_{2.5}$PDs, the ratios of NO_3^-, NH_4^+, and SO_4^{2-} were 0.94, 0.91, and 0.87, respectively, which were much higher than the value of BC (0.79), indicating NO_3^-, NH_4^+, and SO_4^{2-} were quite uniform in the layers of 975–819 hPa with the influence of chemical processes, which is discussed further in Sect. 3.3.4 below.

3.3.4 Process analyses for O_3SPDs, $PM_{2.5}$SPDs, and O_3–$PM_{2.5}$PDs

The process analysis (PA) is applied to identify the relative importance of atmospheric processes in the three types of pollution. Figure 9 shows the net changes in O_3, NO_3^-, NH_4^+, and SO_4^{2-} by the processes of chemical production (Chem), horizontal advection (Horizontal_adv), vertical advection (Vertical_avd), and diffusion (Diff; vertical PBL mixing process) in the GEOS-Chem model, as well as the total of all these processes (i.e., Chem + Diff + Horizontal_avd + Vertical_avd) on O_3SPDs, $PM_{2.5}$SPDs, and O_3–$PM_{2.5}$PDs.

For O_3, the net changes in O_3 by all processes were positive at altitudes of 975–819 hPa on O_3–$PM_{2.5}$PDs and O_3SPDs, in which Chem had the largest positive contribu-

tion (about $1.5\,Gg\,d^{-1}$), indicating O_3 is chemically produced at these layers. For NO_3^- and NH_4^+, the nets of all processes increased mass concentrations at 913–819 hPa on O_3–$PM_{2.5}$PDs and O_3SPDs, in which Chem and Vertical_avd were positive, and Chem had the largest positive contribution. The vertical profiles of Chem were similar for NO_3^- and NH_4^+, both of which had the largest positive values at 913–819 hPa ($2.83\,Gg\,d^{-1}$ for NO_3^- and $0.88\,Gg\,d^{-1}$ for NH_4^+), leading to higher concentrations of NO_3^- and NH_4^+ on O_3–$PM_{2.5}$PDs than on O_3SPDs and $PM_{2.5}$SPDs. Chem and Diff of SO_4^{2-} were different from those of NO_3^- and NH_4^+. For SO_4^{2-}, Chem was positive from the surface to 510 hPa, with a peak around 819 hPa, and Diff was positive at 819–771 hPa but negative from 819 hPa to the surface, which resulted in the uniform SO_4^{2-} profile as shown in Fig. 8. Chem for SO_4^{2-} was the highest around 819 hPa on O_3–$PM_{2.5}$PDs, which was related to the strong liquid-phase chemical formation of SO_4^{2-} (Fig. S7). In addition to Chem, Vertical_avd also had positive contributions to the net changes in O_3, NO_3^-, NH_4^+, and SO_4^{2-} at 944–819 hPa. Vertical_avd was negative at 819 hPa and positive between 944 and 819 hPa, implying that the pollutants were transported from 819 to 944 hPa on O_3–$PM_{2.5}$PDs.

Overall, NO_3^-, NH_4^+, and SO_4^{2-} all had larger chemical productions at 913–819 hPa on O_3–$PM_{2.5}$PDs compared to those on O_3SPDs and $PM_{2.5}$SPDs, accompanied by strong
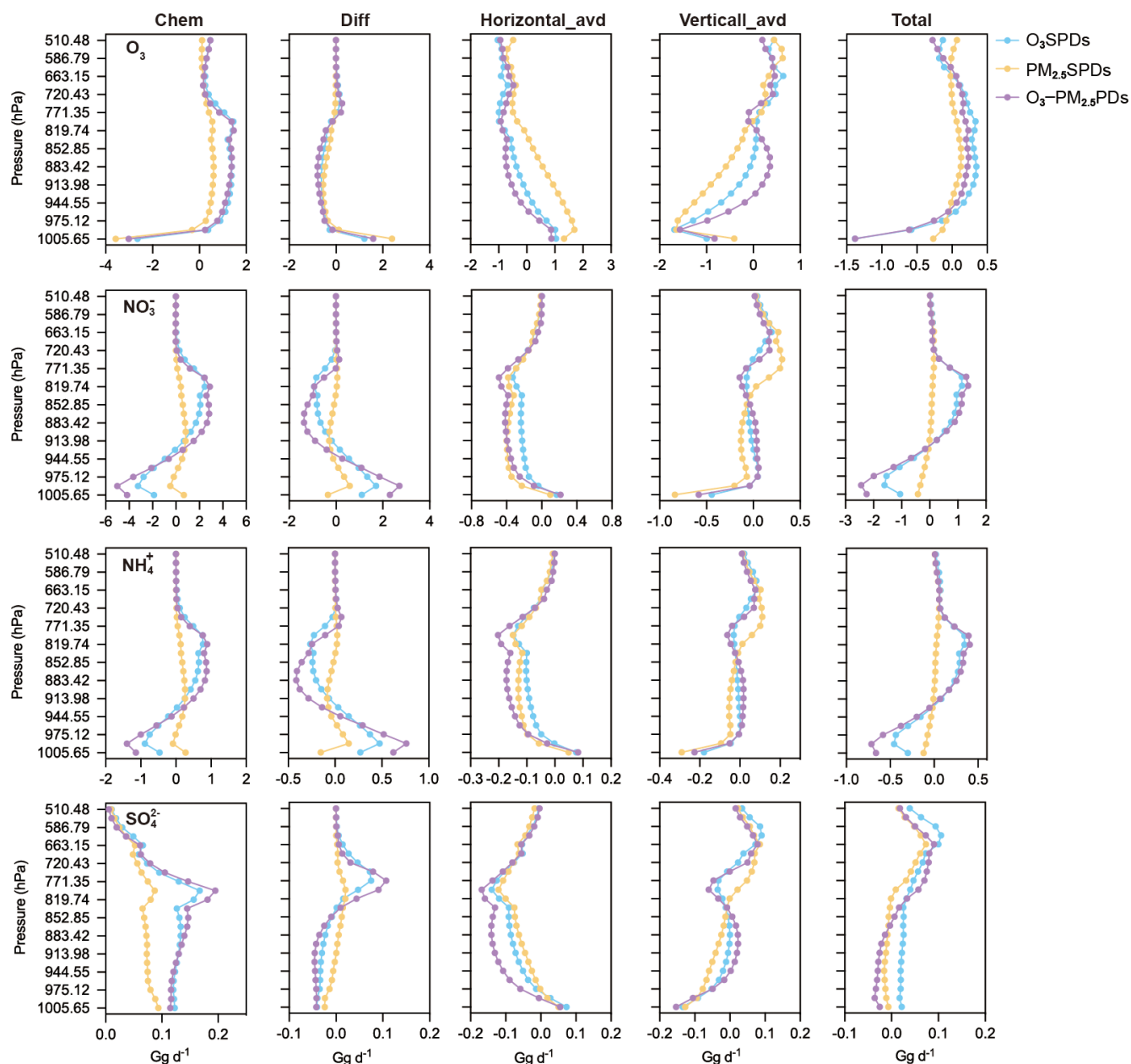
Figure 9. The vertical profiles of net changes in O_3, NO_3^-, NH_4^+, and SO_4^{2-} ($Gg\,d^{-1}$) over BTH by each process and the total processes. The values were averaged over the model-captured regional O_3SPDs, $PM_{2.5}$SPDs, and O_3–$PM_{2.5}$PDs in April–October of 2013–2020.

vertical transport from 819 hPa to near the surface, resulting in the quite uniform vertical profiles at 975–819 hPa on O_3–$PM_{2.5}$PDs. In addition, the vertical profiles of net changes in $PM_{2.5}$ over BTH are shown in Fig. S8 for these three cases. Since NO_3^-, NH_4^+, and SO_4^{2-} were the major components of $PM_{2.5}$, the PA of $PM_{2.5}$ is similar to that of each component.

3.3.5 Observed AOD on O_3SPDs, $PM_{2.5}$SPDs, and O_3–$PM_{2.5}$PDs

To try to support the model result that O_3–$PM_{2.5}$PDs had a more uniform vertical profile than $PM_{2.5}$SPDs from the surface to 819 hPa altitude, we present the scatterplots of observed AOD (at 440 and 675 nm) versus observed $PM_{2.5}$ concentrations on O_3SPDs, $PM_{2.5}$SPDs, and O_3–$PM_{2.5}$PDs in Fig. 10. AERONET observations of AOD from 2013 to 2020 are available at three sites in BTH (Beijing: 39.97° N, 116.38° E; Beijing-CAMS: 39.93° N, 116.31° E; Xianghe:

Figure 10. The scatterplots of **(a)** AOD (440 nm) and **(b)** AOD (675 nm) versus observed $PM_{2.5}$ concentrations on O_3SPDs, $PM_{2.5}$SPDs, and O_3–$PM_{2.5}$PDs in Beijing (39.97° N, 116.38° E) in April–October of 2013–2020.

39.75° N, 116.96° E). At Beijing (39.97° N, 116.38° E), AOD (440 and 675 nm) increased with $PM_{2.5}$ concentration in all three types of pollution. However, under the same levels of surface $PM_{2.5}$ concentration, AOD values on O_3–$PM_{2.5}$PDs were higher than on $PM_{2.5}$SPDs, implying that the column burdens of aerosols were generally higher on O_3–$PM_{2.5}$PDs than on $PM_{2.5}$SPDs, which may support the unique vertical distribution of $PM_{2.5}$ on O_3–$PM_{2.5}$PDs shown in Fig. 8b. The scatterplots at Beijing-CAMS and Xianghe sites are similar and are shown in Fig. S9.

3.4 Meteorological conditions for O_3SPDs, $PM_{2.5}$SPDs, and O_3–$PM_{2.5}$PDs over BTH

Figure 11 shows the vertical profiles of RH, T, and OMEGA for O_3SPDs, $PM_{2.5}$SPDs, and O_3–$PM_{2.5}$PDs captured by the model over BTH in the months of April to October from 2013–2020. It should be noted that O_3–$PM_{2.5}$PDs had an unique vertical distribution of RH. Near the surface, the values of RH on O_3–$PM_{2.5}$PDs were between those on O_3SPDs and $PM_{2.5}$SPDs. However, in the upper layers (883–771 hPa), O_3–$PM_{2.5}$PDs had the highest RH among the three cases, with a peak value of 58.2 %. As a result, the strongest aqueous chemical production of SO_4^{2-} (aqueous oxidation of SO_2 by H_2O_2) occurred on O_3–$PM_{2.5}$PDs around 819 to 771 hPa (Fig. S7). The vertical profiles of temperature were similar in the three types of pollution, with the lowest temperature on $PM_{2.5}$SPDs. The vertical profiles of OMEGA were different in the three cases. On O_3SPDs and O_3–$PM_{2.5}$PDs, OMEGA had positive values around 819 hPa, indicating a strong sinking airflow, leading to a downward transport of pollutants. Under O_3–$PM_{2.5}$PDs, the average values of PBLH and SWGDN were 946.1 m and 257.2 W m^{-2}, respec-

tively, which were higher (lower) than those on $PM_{2.5}$SPDs (O_3SPDs) (Fig. S10).

Figure 12 shows the composited weather patterns for regional O_3SPDs, $PM_{2.5}$SPDs, and O_3–$PM_{2.5}$PDs (over 50 % of the cities in BTH experienced the pollution) that were captured by the model in April–October of 2013–2020. The weather patterns of O_3–$PM_{2.5}$PDs were similar to some extent to those of O_3SPDs but were quite different from those of $PM_{2.5}$SPDs. On O_3–$PM_{2.5}$PDs, the BTH region was controlled by westerlies and an anomalous high-pressure system at 500 hPa (Fig. S11). At 850 hPa, BTH was at the western boundary of an anomalous anticyclone, and the associated strong anomalous southerlies at 850 hPa brought moist air to BTH (Figs. S12 and S13), resulting in a high RH that was beneficial to the aqueous chemical production of SO_4^{2-} on O_3–$PM_{2.5}$PDs. On O_3SPDs, BTH was under the influence of the high-pressure ridge of the western Pacific subtropical high (WPSH) at 850 hPa. Additionally, the northeast cold vortex was located to the southwest of BTH at 850 hPa on O_3SPDs, leading to dry and warm conditions, which was favorable for the formation of O_3. On $PM_{2.5}$SPDs, the BTH region was under the influence of both the continental high and the WPSH at 850 hPa. At the surface, BTH was under the influence of a uniform high pressure with very weak winds and hence stagnate atmosphere, which was conducive to the accumulation of $PM_{2.5}$.

4 Conclusions

We used the observed hourly concentrations of O_3 and $PM_{2.5}$ from CNEMC and the model results from the nested-grid version of the GEOS-Chem model to examine the chemical and physical characteristics of the co-polluted days by
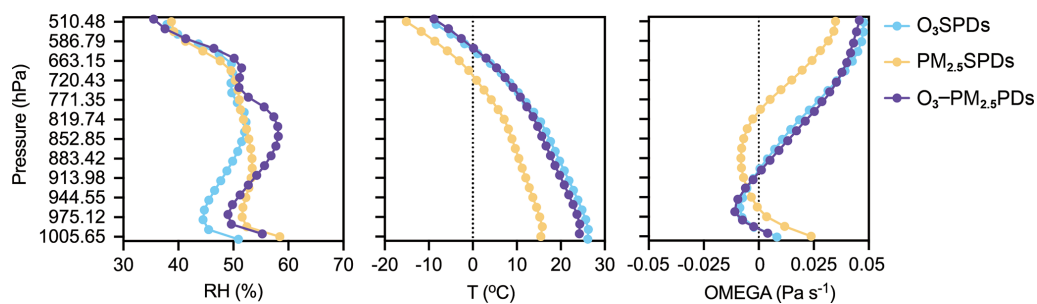
Figure 11. The vertical profiles of RH (%), T (°C), and OMEGA (Pa s⁻¹) averaged over BTH and over the model-captured regional O₃ SPDs, PM₂.₅ SPDs, and O₃–PM₂.₅ PDs in April–October of 2013–2020.
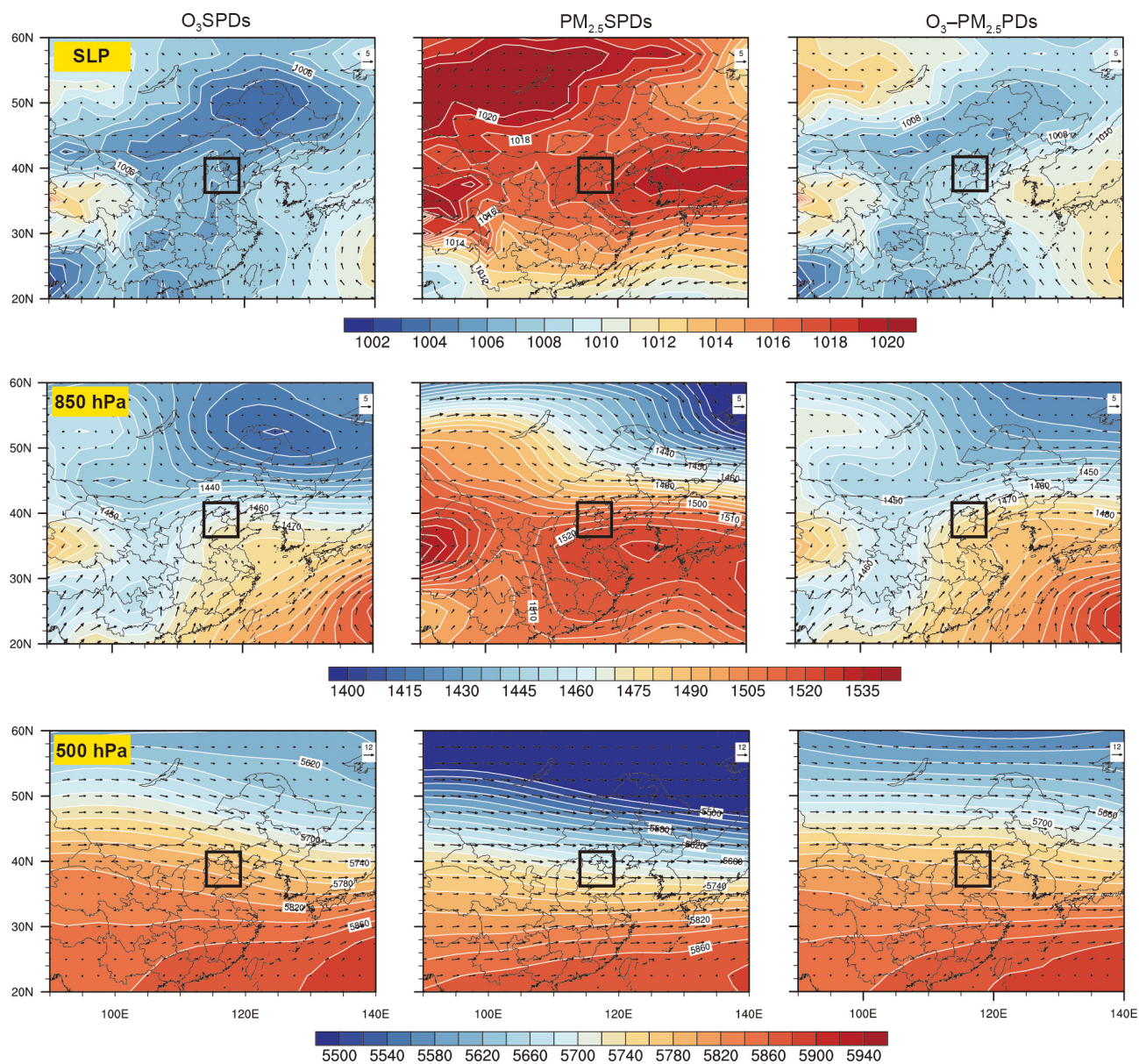

Figure 12. Composites of wind field (m s⁻¹) with SLP (sea level pressure) and with geopotential height at 850 and 500 hPa for regional O₃ SPDs, PM₂.₅ SPDs, and O₃–PM₂.₅ PDs that were captured by the model in April–October of 2013–2020. The solid black rectangle indicates BTH region.
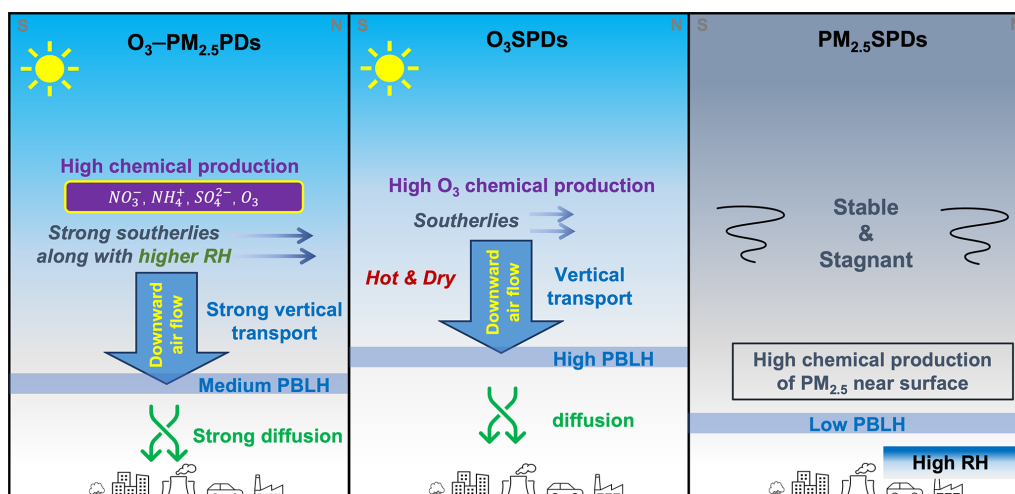
Figure 13. A schematic diagram of chemical and physical and characteristics on O_3SPDs, $PM_{2.5}$SPDs, and O_3–$PM_{2.5}$PDs in BTH region.

O_3 and $PM_{2.5}$ (O_3–$PM_{2.5}$PDs) over the BTH region for eight warm seasons (April–October) from 2013 to 2020. The characteristics of O_3–$PM_{2.5}$PDs were compared with those of the polluted days by O_3 alone (O_3SPDs) and by $PM_{2.5}$ alone ($PM_{2.5}$SPDs). In April–October of 2013–2020, the observed O_3SPDs, $PM_{2.5}$SPDs, and O_3–$PM_{2.5}$PDs were 2954, 2148, and 1614 d, respectively, in which 75.0 % (2954/3937), 58.1 % (2148/3698), and 79.7 % (1614/2024) were captured by the GEOS-Chem model, respectively. We carried out composited analyses of the chemical and physical characteristics for O_3SPDs, $PM_{2.5}$SPDs, and O_3–$PM_{2.5}$PDs by using the samples (days) captured by both the observations and the model.

The chemical characteristics of O_3–$PM_{2.5}$PDs were found to be different from those of O_3SPDs and $PM_{2.5}$SPDs at the surface. O_3–$PM_{2.5}$PDs occurred with high levels of atmospheric oxidants (high OH and O_x), with higher SOR and NOR compared to those on O_3SPDs and $PM_{2.5}$SPDs, leading to high concentrations of both O_3 and $PM_{2.5}$. At the surface, the composited concentrations of NO_3^-, NH_4^+, BC, and OC were the highest on $PM_{2.5}$SPDs, while the composited concentration of SO_4^{2-} was the highest on O_3–$PM_{2.5}$PDs. There was a strong formation of SO_4^{2-} during the daytime on O_3–$PM_{2.5}$PDs in the oxidative atmosphere.

We also found unique features of the vertical distributions of O_3 and $PM_{2.5}$ on O_3–$PM_{2.5}$PDs. Concentrations of $PM_{2.5}$ were stable and high between 975 and 819 hPa on O_3–$PM_{2.5}$PDs, unlike those on $PM_{2.5}$SPDs that decreased rapidly with the altitude. On O_3–$PM_{2.5}$PDs, the vertical profiles of NO_3^-, NH_4^+, and SO_4^{2-} were quite uniform at 975–819 hPa, corresponding to the stable O_3 concentrations at these altitudes. The process analysis (PA) showed that NO_3^-, NH_4^+, and SO_4^{2-} all had larger chemical productions at altitudes of 913–819 hPa on O_3–$PM_{2.5}$PDs compared to those on O_3SPDs and $PM_{2.5}$SPDs. The chemical production of

SO_4^{2-} had large positive values from the surface to about 500 hPa. The Vertical_avd also had positive contributions to the net changes in O_3, NO_3^-, NH_4^+, and SO_4^{2-} at 944–819 hPa on O_3–$PM_{2.5}$PDs. Therefore, the strong chemical productions at 913–819 hPa accompanied by the downward transport resulted in the quite uniform vertical profiles at 975–819 hPa on O_3–$PM_{2.5}$PDs.

Figure 13 summarizes the chemical and physical characteristics on O_3–$PM_{2.5}$PDs, O_3SPDs, and $PM_{2.5}$SPDs in the BTH region. On O_3–$PM_{2.5}$PDs, the strong chemical productions of O_3, NO_3^-, NH_4^+, and SO_4^{2-} occurred at high altitudes of 913–819 hPa, where RH was high, and the accompanied downward airflow caused the stable concentrations at 944–819 hPa. The composited PBLH on O_3–$PM_{2.5}$PDs was about 946.1 m, and the strong mixed diffusion underneath the PBLH led to high concentrations of pollutants at the ground level. In contrast, O_3SPDs occurred in a hot and dry atmosphere with composited PBLH of 1073.5 m. Strong O_3 chemical production occurred around 819 hPa, and O_3 was then transported to the surface by downward airflow. The atmosphere was stable and stagnate when $PM_{2.5}$SPDs occurred, with the lowest PBLH of 681.8 m. High RH (high chemical formation of $PM_{2.5}$) and the accumulation of aerosols led to the highest surface-layer $PM_{2.5}$ on $PM_{2.5}$SPDs.

To summarize, O_3–$PM_{2.5}$PDs were characterized by high O_x, SOR, and NOR; uniform vertical profiles at 975–819 hPa, which were caused by an anomalous high-pressure system at 500 hPa; strong southerlies; and high RH at 850 hPa. Meteorological parameters around 850 hPa promoted strong chemical production of secondary aerosols and downward transport, resulting in the unique vertical profiles and high surface concentrations on O_3–$PM_{2.5}$PDs.

References

AERONET: Aerosol Robotic Network, NASA and LOA-PHOTONS, https://aeronet.gsfc.nasa.gov/new_web/index.html, last access: 17 November 2022.

Alexander, B., Park, R. J., Jacob, D. J., Li, Q. B., Yantosca, R. M., Savarino, J., Lee, C. C. W., and Thiemens, M. H.: Sulfate formation in sea-salt aerosols: Constraints from oxygen isotopes, J. Geophys. Res.-Atmos., 110, D10307, https://doi.org/10.1029/2004jd005659, 2005.

Atmospheric Chemistry Modeling group: GEOS-Chem model: the Goddard Earth Observing System-Chemisty model, Harvard University, http://acmg.seas.harvard.edu, last access: 17 November 2022.

Bey, I., Jacob, D. J., Yantosca, R. M., Logan, J. A., Field, B. D., Fiore, A. M., Li, Q. B., Liu, H. G. Y., Mickley, L. J., and Schultz, M. G.: Global modeling of tropospheric chemistry with assimilated meteorology: Model description and evaluation, J. Geophys. Res.-Atmos., 106, 23073–23095, https://doi.org/10.1029/2001jd000807, 2001.

Chinese State Council: Action Plan on Air Pollution Prevention and Control, http://www.gov.cn/zwgk/2013-09/12/content_2486773.htm (last access: 24 December 2022), 2013 (in Chinese).

Chinese State Council: Three-Year Action Plan on Defending the Blue Sky, http://www.gov.cn/zhengce/content/2018-07/03/content_5303158.htm (last access: 24 December 2022), 2018 (in Chinese).

Chu, B. W., Ma, Q. X., Liu, J., Ma, J. Z., Zhang, P., Chen, T. A., Feng, Q. C., Wang. C. Y., Yang, N., Ma, H. N., Ma, J. J., Russell, A. G., and He, H.: Air Pollutant Correlations in China: Secondary Air Pollutant Responses to NO_x and SO_2 Control, Environ. Sci. Tech. Let., 7, 695–700, https://doi.org/10.1021/acs.estlett.0c00403, 2020.

CNEMC: China National Environmental Monitoring Center, http://www.cnemc.cn, last access: 24 December 2022 (in Chinese).

Dai, H. B., Zhu, J., Liao, H., Li, J. D., Liang, M. X., Yang, Y., and Yue, X.: Co-occurrence of ozone and $PM_{2.5}$ pollution in the Yangtze River Delta over 2013–2019: spatiotemporal distribution and meteorological conditions, Atmos. Res., 249, 105363, https://doi.org/10.1016/j.atmosres.2020.105363, 2021.

Dang, R. and Liao, H.: Severe winter haze days in the Beijing–Tianjin–Hebei region from 1985 to 2017 and the roles of anthropogenic emissions and meteorology, Atmos. Chem. Phys., 19, 10801–10816, https://doi.org/10.5194/acp-19-10801-2019, 2019.

Dang, R. J., Liao, H., and Fu, Y.: Quantifying the anthropogenic and meteorological influences on summertime surface ozone in China over 2012–2017, Sci. Total. Environ., 754, 142394, https://doi.org/10.1016/j.scitotenv.2020.142394, 2021.

Duan, F., He, K., Ma, Y., Yang, F., Yu, X., Cadle, S. H., Chan, T., and Mulawa, P. A.: Concentration and chemical characteristics of $PM_{2.5}$ in Beijing, China: 2001–2002, Sci. Total Environ., 355, 264–275, https://doi.org/10.1016/j.scitotenv.2005.03.001, 2006.

Fairlie, T. D., Jacob, D. J., and Park, R. J.: The impact of transpacific transport of mineral dust in the United States, Atmos. Environ., 41, 1251–1266, https://doi.org/10.1016/j.atmosenv.2006.09.048, 2007.

Gao, Y. and Ji, H. B.: Microscopic morphology and seasonal variation of health effect arising from heavy metals in $PM_{2.5}$ and PM_{10}: One-year measurement in a densely populated area of urban Beijing, Atmos. Res., 212, 213–226, https://doi.org/10.1016/j.atmosres.2018.04.027, 2018.

Giles, D. M., Sinyuk, A., Sorokin, M. G., Schafer, J. S., Smirnov, A., Slutsker, I., Eck, T. F., Holben, B. N., Lewis, J. R., Campbell, J. R., Welton, E. J., Korkin, S. V., and Lyapustin, A. I.: Advancements in the Aerosol Robotic Network (AERONET) Version 3

database – automated near-real-time quality control algorithm with improved cloud screening for Sun photometer aerosol optical depth (AOD) measurements, Atmos. Meas. Tech., 12, 169–209, https://doi.org/10.5194/amt-12-169-2019, 2019.

Gonçalves, M., Jiménez-Guerrero, P., and Baldasano, J. M.: Contribution of atmospheric processes affecting the dynamics of air pollution in South-Western Europe during a typical summertime photochemical episode, Atmos. Chem. Phys., 9, 849–864, https://doi.org/10.5194/acp-9-849-2009, 2009.

Gong, C. and Liao, H.: A typical weather pattern for ozone pollution events in North China, Atmos. Chem. Phys., 19, 13725–13740, https://doi.org/10.5194/acp-19-13725-2019, 2019.

Gong, C., Liao, H., Zhang, L., Yue, X., Dang, R. J., and Yang, Y.: Persistent ozone pollution episodes in North China exacerbated by regional transport, Environ. Pollut., 265, 115056, https://doi.org/10.1016/j.envpol.2020.115056, 2020.

Guenther, A. B., Jiang, X., Heald, C. L., Sakulyanontvittaya, T., Duhl, T., Emmons, L. K., and Wang, X.: The Model of Emissions of Gases and Aerosols from Nature version 2.1 (MEGAN2.1): an extended and updated framework for modeling biogenic emissions, Geosci. Model Dev., 5, 1471–1492, https://doi.org/10.5194/gmd-5-1471-2012, 2012.

Jiang, N., Li, L., Wang, S., Li, Q., Dong, Z., Duan, S., Zhang, R., and Li, S.: Variation tendency of pollution characterization, sources, and health risks of $PM_{2.5}$-bound polycyclic aromatic hydrocarbons in an emerging megacity in China: based on three-year data, Atmos. Res., 217, 81–92, https://doi.org/10.1016/j.atmosres.2018.10.023, 2019.

Li, K., Jacob, D. J., Liao, H., Zhu, J., Shah, V., Shen, L., Bates, K., Zhang, Q., and Zhai, S. X.: A two-pollutant strategy for improving ozone and particulate air quality in China, Nat. Geosci., 12, 906–910, https://doi.org/10.1038/s41561-019-0464-x, 2019.

Li, K., Jacob, D. J., Shen, L., Lu, X., De Smedt, I., and Liao, H.: Increases in surface ozone pollution in China from 2013 to 2019: anthropogenic and meteorological influences, Atmos. Chem. Phys., 20, 11423–11433, https://doi.org/10.5194/acp-20-11423-2020, 2020.

Li, M., Zhang, Q., Kurokawa, J.-I., Woo, J.-H., He, K., Lu, Z., Ohara, T., Song, Y., Streets, D. G., Carmichael, G. R., Cheng, Y., Hong, C., Huo, H., Jiang, X., Kang, S., Liu, F., Su, H., and Zheng, B.: MIX: a mosaic Asian anthropogenic emission inventory under the international collaboration framework of the MICS-Asia and HTAP, Atmos. Chem. Phys., 17, 935–963, https://doi.org/10.5194/acp-17-935-2017, 2017.

Li, M., Wang, L., and Liu, J.: Exploring the regional pollution characteristics and meteorological formation mechanism of $PM_{2.5}$ in North China during 2013–2017, Environ. Int., 134, 105283, https://doi.org/10.1016/j.envint.2019.105283, 2019.

Liu, Y. X., Zhao, Q. B., Hao, X., Zhao, J. R., Zhang, Y., Yang, X., Fu, Q. Y., Xu, X. Y., Wang, X. F., Huo, J. T., and Chen, J. M.: Increasing surface ozone and enhanced secondary organic carbon formation at a city junction site: An epitome of the Yangtze River Delta, China (2014–2017), Environ. Pollut., 265, 0269-7491, https://doi.org/10.1016/j.envpol.2020.114847, 2020.

Lou, S. J., Liao, H., Yang, Y., and Mu, Q.: Simulation of the interannual variations of tropospheric ozone over China: Roles of variations in meteorological parameters and anthropogenic emissions, Atmos. Environ., 122, 839–851, https://doi.org/10.1016/j.atmosenv.2015.08.081, 2015.

Molod, A., Takacs, L., Suarez, M., and Bacmeister, J.: Development of the GEOS-5 atmospheric general circulation model: evolution from MERRA to MERRA2, Geosci. Model Dev., 8, 1339–1356, https://doi.org/10.5194/gmd-8-1339-2015, 2015.

Mu, Q. and Liao, H.: Simulation of the interannual variations of aerosols in China: role of variations in meteorological parameters, Atmos. Chem. Phys., 14, 9597–9612, https://doi.org/10.5194/acp-14-9597-2014, 2014.

Nan, J. L., Wang, S. S., Guo, Y. L., Xiang, Y. J., and Zhou, B.: Study on the daytime OH radical and implication for its relationship with fine particles over megacity of Shanghai, China, Atmos. Environ., 154, 167–178, https://doi.org/10.1016/j.atmosenv.2017.01.046, 2017.

Ni, R., Lin, J., Yan, Y., and Lin, W.: Foreign and domestic contributions to springtime ozone over China, Atmos. Chem. Phys., 18, 11447–11469, https://doi.org/10.5194/acp-18-11447-2018, 2018.

Park, R. J., Jacob, D. J., Chin, M., and Martin, R. V.: Sources of carbonaceous aerosols over the United States and implications for natural visibility, J. Geophys. Res.-Atmos., 108, 4355, https://doi.org/10.1029/2002jd003190, 2003.

Park, R. J., Jacob, D. J., Field, B. D., Yantosca, R. M., and Chin, M.: Natural and transboundary pollution influences on sulfate-nitrate-ammonium aerosols in the United States: Implications for policy, J. Geophys. Res.-Atmos., 109, D15204, https://doi.org/10.1029/2003jd004473, 2004.

Pye, H. O. T., Liao, H., Wu, S., Mickley, L. J., Jacob, D. J., Henze, D. K., and Seinfeld, J. H.: Effect of changes in climate and emissions on future sulfate-nitrate-ammonium aerosol levels in the United States, J. Geophys. Res.-Atmos., 114, D01205, https://doi.org/10.1029/2008jd010701, 2009.

Qin, Y., Li, J. Y., Gong, K. J., Wu, Z., Chen, M. D., Qin, M. M., Huang, L., and Hu, J. L.: Double high pollution events in the Yangtze River Delta from 2015 to 2019: Characteristics, trends, and meteorological situations, Sci. Total. Environ., 792, 148349, https://doi.org/10.1016/j.scitotenv.2021.148349, 2021.

Ren, W., Tian, H., Tao, B., Chappelka, A., Sun, G., Lu, C., Liu, M., Chen, G., and Xu, X.: Impacts of tropospheric ozone and climate change on net primary productivity and net carbon exchange of China's forest ecosystems, Glob. Ecol. Biogeogr., 20, 391–406, https://doi.org/10.1111/j.1466-8238.2010.00606.x, 2011.

Sun, T., Wu, C., and Wu, D.: Time-resolved black carbon aerosol vertical distribution measurements using a 356-m meteorological tower in Shenzhen, Theor. Appl. Climatol., 140, 1263–1276, https://doi.org/10.1007/s00704-020-03168-6, 2020.

Tan, Z., Fuchs, H., Lu, K., Hofzumahaus, A., Bohn, B., Broch, S., Dong, H., Gomm, S., Häseler, R., He, L., Holland, F., Li, X., Liu, Y., Lu, S., Rohrer, F., Shao, M., Wang, B., Wang, M., Wu, Y., Zeng, L., Zhang, Y., Wahner, A., and Zhang, Y.: Radical chemistry at a rural site (Wangdu) in the North China Plain: observation and model calculations of OH, HO_2 and RO_2 radicals, Atmos. Chem. Phys., 17, 663–690, https://doi.org/10.5194/acp-17-663-2017, 2017.

Wang, H., Kiang, C., Tang, X., Zhou, X., and Chameides, W. L.: Surface ozone: a likely threat to crops in Yangtze delta of China, Atmos. Eviron., 39, 3843–3850, https://doi.org/10.1016/j.atmosenv.2005.02.057, 2005.

Wang, X., Manning, W., Feng, Z., and Zhu, Y.: Ground-level ozone in China: distribution and effects on crop yields, Environ. Pollut.,

147, 394–400, https://doi.org/10.1016/j.envpol.2006.05.006, 2007.

Woodward-Massey, R., Slater, E. J., Alen, J., Ingham, T., Cryer, D. R., Stimpson, L. M., Ye, C., Seakins, P. W., Whalley, L. K., and Heard, D. E.: Implementation of a chemical background method for atmospheric OH measurements by laser-induced fluorescence: characterisation and observations from the UK and China, Atmos. Meas. Tech., 13, 3119–3146, https://doi.org/10.5194/amt-13-3119-2020, 2020.

Xuan, J., Liu, G., and Du, K.: Dust emission inventory in northern China, Atmos. Environ., 34, 4565–4570, https://doi.org/10.1016/S1352-2310(00)00203-X, 2000.

Ye, B., Ji, X., Yang, H., Yao, X., Chan, C. K., Cadle, S. H., Chan, T., and Mulawa, P. A.: Concentration and chemical composition of PM₂.₅ in Shanghai for a 1-year period, Atmos. Environ., 37, 499–510, https://doi.org/10.1016/S1352-2310(02)00918-4, 2003.

Yue, X., Unger, N., Harper, K., Xia, X., Liao, H., Zhu, T., Xiao, J., Feng, Z., and Li, J.: Ozone and haze pollution weakens net primary productivity in China, Atmos. Chem. Phys., 17, 6073–6089, https://doi.org/10.5194/acp-17-6073-2017, 2017.

Zhang, Y. and Wang, Y.: Climate-driven ground-level ozone extreme in the fall over the Southeast United States, P. Natl. Acad. Sci. USA, 113, 10025–10030, https://doi.org/10.1073/pnas.1602563113, 2016.

Zhao, X. J., Zhao, P. S., Xu, J., Meng,, W., Pu, W. W., Dong, F., He, D., and Shi, Q. F.: Analysis of a winter regional haze event and its formation mechanism in the North China Plain, Atmos. Chem. Phys., 13, 5685–5696, https://doi.org/10.5194/acp-13-5685-2013, 2013.

Zheng, B., Tong, D., Li, M., Liu, F., Hong, C., Geng, G., Li, H., Li, X., Peng, L., Qi, J., Yan, L., Zhang, Y., Zhao, H., Zheng, Y., He, K., and Zhang, Q.: Trends in China's anthropogenic emissions since 2010 as the consequence of clean air actions, Atmos. Chem. Phys., 18, 14095–14111, https://doi.org/10.5194/acp-18-14095-2018, 2018.

Zheng, B., Zhang, Q., Geng, G., Chen, C., Shi, Q., Cui, M., Lei, Y., and He, K.: Changes in China's anthropogenic emissions and air quality during the COVID-19 pandemic in 2020, Earth Syst. Sci. Data, 13, 2895–2907, https://doi.org/10.5194/essd-13-2895-2021, 2021.

Zhu, J., Chen, L., Liao, H., and Dang, R. J.: Correlations between PM₂.₅ and ozone over China and associated underlying reasons, Atmosphere, 10, 352, https://doi.org/10.3390/atmos10070352, 2019.

Zong, L., Yang, Y., Gao, M., Wang, H., Wang, P., Zhang, H., Wang, L., Ning, G., Liu, C., Li, Y., and Gao, Z.: Large-scale synoptic drivers of co-occurring summertime ozone and PM₂.₅ pollution in eastern China, Atmos. Chem. Phys., 21, 9105–9124, https://doi.org/10.5194/acp-21-9105-2021, 2021.